

MAGNETIC FIELD DISTRIBUTION AND LEVITATION FORCE CALCULATION IN HTSC-PMG MAGLEV VEHICLES

Kamel Boughrara^{1, *} and Rachid Ibtouen²

¹Laboratoire de l'Energie et des Systèmes Intelligents (LESI), Université de Khemis-Miliana, Route de Theniet El-had, Khemis-Miliana 44225, Algeria

²Ecole Nationale Polytechnique (LRE-ENP), Algiers, 10, Av. Pasteur, El Harrach, BP182, 16200, Algeria

Abstract—This paper presents a new analytical method for predicting magnetic field distribution and levitation force in three configurations of high temperature superconducting (HTSC) maglev vehicles. The permanent magnet guideways (PMG) are composed with ferromagnetic materials and NdFeB permanent magnets. The proposed analytical model is based on the resolution in each region of Laplace's and Poisson's equations by using the technique of separation of variables. For the study, we consider the HTSC as a perfect diamagnetic material. The boundary conditions and Fourier series expansion of interfaces conditions between each region are used to find the solution of magnetic field. The developed analytical method is extended to compute the magnetic field distribution generated by the three types of PMGs when removing the HTSC bulk. Magnetic field distribution and vertical force obtained analytically are compared with those issued from the finite element method (FEM).

1. INTRODUCTION

Magnetic levitation (maglev) is widely used in many applications such as superconducting magnetic bearings (SMB), energy storage system and flywheels, magnetic levitating vehicle. Compared with the conventional active controlled electromagnetic levitation system, the passive HTSC maglev system has many advantages, such as self stabilization, low cost, high levitation height, and high reliability [1–9].

Received 27 August 2013, Accepted 22 September 2013, Scheduled 24 September 2013

* Corresponding author: Kamel Boughrara (boughrarakamel@yahoo.fr).

Much work has been done with considering the superconductor as a perfect diamagnetic material to determine the levitation force in SMB, the thrust force in magnetic gear and the electromagnetic torque in superconducting reluctance machine. This consideration implies an evaluated force in SMB greater than the real levitation force [10–15].

The knowledge of optimal PMG and HTSC dimensions is essential to design SMB for various applications. The most important parameter of a SMB is the developed levitation force between the superconductor and the magnetic source (PMG) [16–18]. Many authors used Biot-Savart law for the calculation and optimization of magnetic field distribution in the PMG alone without taking into account the ferromagnetic material [1, 7, 19, 20]. Static finite element method is also used for the prediction of magnetic field generated by the PMG alone. The levitation force in real HTSC-PMG is computed by Lorentz force formula and finite element method using bean model or flux flow-creep model. The flux density generated by the PMG alone and calculated with Biot-Savart law or static FEM is used as excitation field in the finite element method [1, 18, 21–23]. In [24], the author used a numerical Schwartz-Christoffel (NSC) method to predict magnetic field distribution and levitation force in diamagnetic bearings. The analytical method presented in our paper which is more accurate than Biot-Savart law and NSC mapping, can be coupled to finite element method to determine levitation force for real HTSC-PMG systems at the second stage of design of SMB.

The proposed analytical method which is based on the subdomain model [25, 26] and boundary value problems is used to predict the magnetic field distribution and levitation force in HTSC-PMG maglev vehicles. Three configurations which have been extensively analyzed numerically (FEM) and experimentally [27–30] are considered in this paper. Moreover, the magnetic field distribution created by the three configurations of PMG alone is also determined with the developed analytical method. In order to validate the proposed model, the results are compared with those obtained from finite element method (FEM) [31].

2. MAGNETIC FIELD SOLUTION IN HTSC-PMG MAGLEV VEHICLES

Here, we propose an analytical solution of the magnetic field distribution in the studied HTSC-PMG maglev vehicles.

Figure 1 shows the model of the HTSC-PMG (Geometry A) maglev vehicle formulated in two-dimensional Cartesian coordinates with assuming the axial length of the machine infinite, i.e., end effects

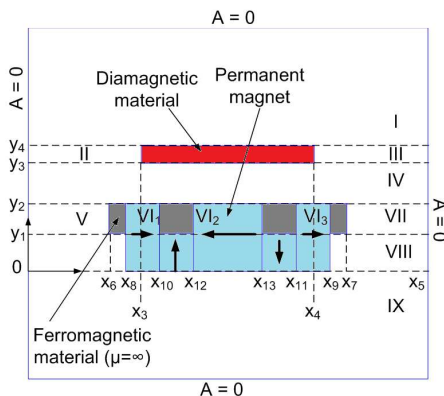


Figure 1. HTSC-PMG model: Geometry A.

are neglected. The partial differential equations for magnetic field in term of vector potential A which has only one component in the z direction and is not dependent on the z coordinate, can be expressed by

$$\frac{\partial^2 A(x, y)}{\partial x^2} + \frac{\partial^2 A(x, y)}{\partial y^2} = 0 \quad (1)$$

in regions I, II, III, IV, V, VI, VII and IX.

$$\frac{\partial^2 A(x, y)}{\partial x^2} + \frac{\partial^2 A(x, y)}{\partial y^2} = -\mu_0 \frac{d}{dx} M_y(x) \quad (2)$$

in region VIII, where $M_y(x) = M1_y(x) + M2_y(x)$ and $M1_y(x)$ and $M2_y(x)$ are the magnetization in the y direction of permanent magnets. The field vectors B and H , in the different regions, are coupled by

$$\vec{B} = \mu_0 \vec{H}, \quad \text{in regions I, II, III, IV, V, VII and IX} \quad (3)$$

where $B_y(x, y) = \mu_0 H_y(x, y)$ and $B_x(x, y) = \mu_0 H_x(x, y)$

$$\vec{B} = \mu_0 \mu_r \vec{H} + \mu_0 \vec{M}, \quad \text{in regions VI and VIII} \quad (4)$$

where $B_{j,y}(x, y) = \mu_0 \mu_r H_{j,y}(x, y)$ and $B_{j,x}(x, y) = \mu_0 \mu_r H_{j,x}(x, y) + \mu_0 M_{j,x}(x)$ and $M_{j,x}(x)$ (j vary from 1 to 3) is the magnetization in the x direction of permanent magnets in region VI, and μ_r is the relative recoil permeability of permanent magnets which is set to unity.

In region VI, the magnetization distribution in x -direction of horizontally magnetized permanent magnets is given as

$$M_x(x) = \left[\frac{B_r}{\mu_0} \quad -\frac{B_r}{\mu_0} \quad \frac{B_r}{\mu_0} \right] \quad (5)$$

where B_r is the residual magnetization of permanent magnets.

In region VIII, $B_y(x, y) = \mu_0\mu_r H_y(x, y) + \mu_0 M_y(x)$ and $B_x(x, y) = \mu_0\mu_r H_x(x, y) + \mu_0 M_x(x)$, where $M_x(x) = M1_x(x) + M2_x(x) + M3_x(x)$ and $M1_x(x)$, $M2_x(x)$ and $M3_x(x)$ are the magnetization in the x direction of permanent magnets.

Flux density components are deduced from A by

$$B_y(x, y) = -\frac{\partial A(x, y)}{\partial x}, \quad B_x(x, y) = \frac{\partial A(x, y)}{\partial y} \quad (6)$$

Compared to real HTS bulk, the flux lines in a perfect diamagnetic behavior of the HTS bulk is totally rejected from the HTS bulk and the flux lines are tangential to the surface of the bulk.

As shown in Fig. 1, the whole domain is divided into nine sub-domains (regions) where the perfect diamagnetic material is equivalent to imposing a Dirichlet condition on the surfaces of the superconducting bulk:

$$\begin{cases} A(x_3, y) = 0 & y_3 < y < y_4 \\ A(x_4, y) = 0 & y_3 < y < y_4 \\ A(x, y_3) = 0 & x_3 < x < x_4 \\ A(x, y_4) = 0 & x_3 < x < x_4 \end{cases} \quad (7)$$

The infinitely permeable ferromagnetic material is equivalent for example to imposing

$$\begin{cases} B_y(x_6, y) = 0 & y_1 < y < y_2 \\ B_y(x_8, y) = 0 & y_1 < y < y_2 \\ H_x(x, y_1) = 0 & x_6 < x < x_8 \\ H_x(x, y_2) = 0 & x_6 < x < x_8 \end{cases} \quad (8)$$

The whole domain is limited in the x coordinate direction ($x = 0$ and $x = x_5$), where homogeneous Dirichlet boundary conditions have been imposed ($A = 0$). These outer boundaries must be chosen sufficiently far away from the area where reliable solutions are needed so that they do not affect the results ($x_6 \gg 0$ and $x_5 \gg x_7$). Moreover, the magnetic vector potential in regions I and IX must be finite at $y = \infty$ and $y = -\infty$, respectively.

The magnetization components $M1_x(x)$, $M2_x(x)$, $M3_x(x)$, $M1_y(x)$ and $M2_y(x)$ in region VIII are independent of the y -coordinate and depends only on the x -coordinate as shown in Fig. 2.

The source terms $M1_x(x)$, $M2_x(x)$ and $M3_x(x)$ can be expanded as

$$M1_x(x) = \sum_{n=1}^{\infty} M1x_n \sin(\alpha x) \quad (9)$$

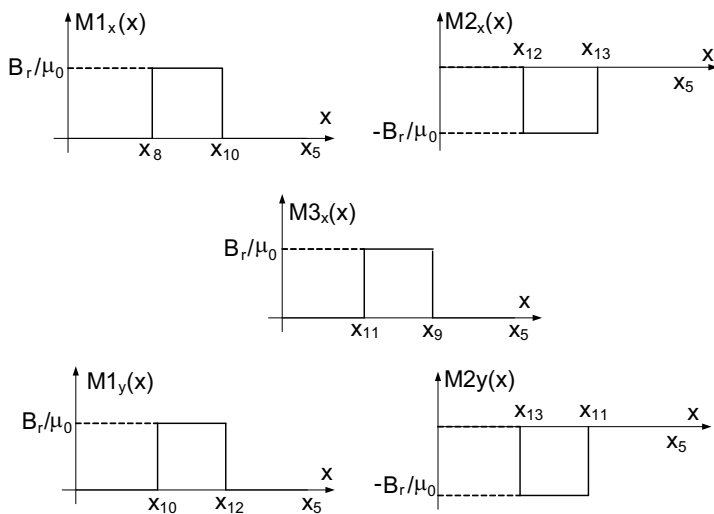


Figure 2. Tangential and radial magnetization distributions in region VIII.

where $M1x_n = \frac{2}{x_5} \int_{x_8}^{x_{10}} \frac{B_r}{\mu_0} \sin(\alpha x) dx$ where n is a positive integer and $\alpha = \frac{n\pi}{x_5}$.

$$M2_x(x) = \sum_{n=1}^{\infty} M2x_n \sin(\alpha x) \tag{10}$$

where $M2x_n = -\frac{2}{x_5} \int_{x_{12}}^{x_{13}} \frac{B_r}{\mu_0} \sin(\alpha x) dx$.

$$M3_x(x) = \sum_{n=1}^{\infty} M3x_n \sin(\alpha x) \tag{11}$$

where $M3x_n = \frac{2}{x_5} \int_{x_{11}}^{x_9} \frac{B_r}{\mu_0} \sin(\alpha x) dx$.

The source terms represented by the radial magnetization distributions $M1_y(x)$ and $M2_y(x)$ are expanded as

$$M1_y(x) = M1y_0 + \sum_{n=1}^{\infty} M1y_n \cos(\alpha x) \tag{12}$$

where $M1y_0 = \frac{1}{x_5} \int_{x_{10}}^{x_{12}} \frac{B_r}{\mu_0} dx$ and $M1y_n = \frac{2}{x_5} \int_{x_{10}}^{x_{12}} \frac{B_r}{\mu_0} \cos(\alpha x) dx$.

$$M2_y(x) = M2y_0 + \sum_{n=1}^{\infty} M2y_n \cos(\alpha x) \tag{13}$$

where $M2y_0 = -\frac{1}{x_5} \int_{x_{13}}^{x_{11}} \frac{B_r}{\mu_0} dx$ and $M2y_n = -\frac{2}{x_5} \int_{x_{13}}^{x_{11}} \frac{B_r}{\mu_0} \cos(\alpha x) dx$.

The partial differential Equations (1) and (2) issued from Maxwell's equations are solved in each region (Fig. 1) by using the method of separation of variables and Fourier series analysis.

In region I, which is delimited in y -direction by $y = y_4$ and $y = +\infty$ and in x -direction by $x = 0$ and $x = x_5$, we have to solve the Laplace equation. Considering the Dirichlet conditions at $x = 0$ and $x = x_5$ and the magnetic vector potential finite at $y = +\infty$, the general solution of (1) can be expressed as

$$AI(x, y) = \sum_{n=1}^{\infty} C1_n e^{-\alpha y} \sin(\alpha x) \quad (14)$$

The regions II and III are delimited in the y -direction by $y = y_4$ and $y = y_3$ and satisfies the Dirichlet conditions at $x = 0$, $x = x_3$, $x = x_4$ and $x = x_5$. From boundary conditions (7), the solutions of (1) in regions II and III are:

$$AII(x, y) = \sum_{k=1}^{\infty} \left(C2_k e^{\beta y} + C3_k e^{-\beta y} \right) \sin(\beta x) \quad (15)$$

in region II, where $\beta = \frac{k\pi}{x_3}$ and k a positive integer.

$$AIII(x, y) = \sum_{k=1}^{\infty} \left(C4_k e^{\lambda y} + C5_k e^{-\lambda y} \right) \sin(\lambda(x - x_4)) \quad (16)$$

in region III, where $\lambda = \frac{k\pi}{x_5 - x_4}$.

The air gap between the superconducting bulk and permanent magnet guideway is represented by the region IV. It is delimited in the y -direction by $y = y_3$ and $y = y_2$. From the Dirichlet conditions at $x = 0$ and $x = x_5$, the solution of Laplace's Equation (1) in IV is given as

$$AIV(x, y) = \sum_{n=1}^{\infty} \left(C6_n e^{\alpha y} + C7_n e^{-\alpha y} \right) \sin(\alpha x) \quad (17)$$

The permanent magnet guideway is composed by permanent magnets magnetized in y -direction and x -direction and ferromagnetic material. The presence of iron introduces in the HTSC-PMG model the boundary conditions (8). The resolution of Laplace's Equation (1) in regions V, VI and VII by using the technique of separation of variables permits to get

$$AV(x, y) = \sum_{l=0}^{\infty} \left(C8_l e^{\psi y} + C9_l e^{-\psi y} \right) \sin(\psi x) \quad (18)$$

in region V, where $\psi = \frac{(2l+1)\pi}{2x_6}$ and l an integer.

$$AVI_j(x, y) = C10_{j,0} + C11_{j,0}y + \sum_{m=1}^{\infty} (C10_{j,m}e^{-\eta_j y} + C11_{j,m}e^{\eta_j y}) \cos\left(\eta_j\left(x - g_j + \frac{c_j}{2}\right)\right) \quad (19)$$

in region VI, where $g = \left[x_8 + \frac{x_{10}-x_8}{2} \quad x_{12} + \frac{x_{13}-x_{12}}{2} \quad x_{11} + \frac{x_9-x_{11}}{2} \right]$, $c = [x_{10} - x_8 \quad x_{13} - x_{12} \quad x_9 - x_{11}]$ and $\eta_j = \frac{m\pi}{c_j}$.

$$AVII(x, y) = \sum_{l=0}^{\infty} (C12_l e^{\omega y} + C13_l e^{-\omega y}) \cos(\omega(x - x_7)) \quad (20)$$

in region VII, where $\omega = \frac{(2l+1)\pi}{2(x_5-x_7)}$.

Region VIII is delimited in y -direction by $y = 0$ and $y = y_1$ and in x -direction by $x = 0$ and $x = x_5$. From boundary conditions in x -direction, the general solution of magnetic vector potential governed by the Poisson Equation (2) is given as

$$AVIII(x, y) = \sum_{n=1}^{\infty} \left(C14_n e^{\alpha y} + C15_n e^{-\alpha y} - \frac{My_n \mu_0}{\alpha} \right) \sin(\alpha x) \quad (21)$$

where $My_n = M1y_n + M2y_n$.

In region IX, which is delimited in y -direction by $y = 0$ and $y = -\infty$ and in x -direction by $x = 0$ and $x = x_5$, we have to solve the Laplace equation. Considering the Dirichlet conditions at $x = 0$ and $x = x_5$ and the magnetic vector potential finite at $y = -\infty$, the general solution of (1) can be expressed as

$$AIX(x, y) = \sum_{n=1}^{\infty} C16_n e^{\alpha y} \sin(\alpha x) \quad (22)$$

The relations between the integration constants $C1_n, C2_k, C3_k, C4_k, C5_k, C6_n, C7_n, C8_l, C9_l, C10_{j,0}, C10_{j,m}, C11_{j,0}, C11_{j,m}, C12_l, C13_l, C14_n, C15_n$ and $C16_n$ are determined by applying the interface conditions between the different regions. The system of equations issued from the interface conditions is given in the appendix. It is important to notice that the continuity conditions of the regions of HTSC bulk are different to those of permanent magnets guideway.

The developed analytical method is used to predict magnetic field distribution and levitation force in HTSC-PMG maglev vehicles (geometries B and C) where the PMG are composed with ferromagnetic materials and horizontally magnetized permanent magnets. The

model of both studied configurations with the corresponding nine sub-domains is shown in Fig. 3. The methodology and developments are identical to above HTSC-PMG (Geometry A). However, only Laplace Equation (1) is solved in all sub-domains by using the method of separation of variables.

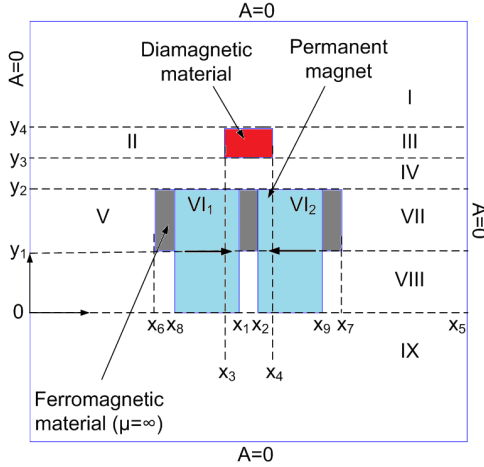


Figure 3. HTSC-PMG model for geometries B and C.

3. MAGNETIC FIELD CREATED BY THE PMG ALONE

Nowadays, the prediction and optimization of magnetic field distribution generated by the PMG alone is obtained numerically using static FEM or analytically using Biot-Savart law. The Biot-Savart law does not take into account the ferromagnetic material. The obtained magnetic flux density is used as excitation field in the finite element method using bean model or flux flow-creep model of real HTSC bulk (type-II superconductors). In this section, we extend the developed analytical method to compute magnetic field distribution generated by the PMGs alone. For Geometry A, the model of PMG alone (Fig. 4) is obtained with removing regions II, III and IV from the model of HTSC-PMG model of Fig. 1. The study is done as above with solving Equations (1) and (2) by using the method of separation of variables.

The model of Fig. 5 is used to predict magnetic field distribution developed by the PMGs alone (geometries B and C). This is done with solving only Laplace's Equation (1) in each region using the method of separation of variables.

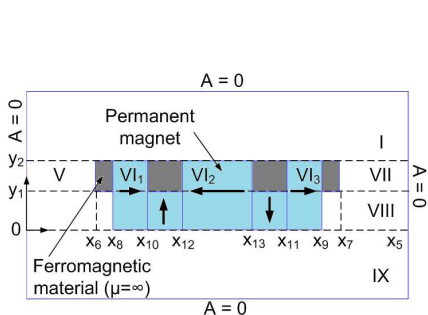


Figure 4. PMG model (Geometry A).

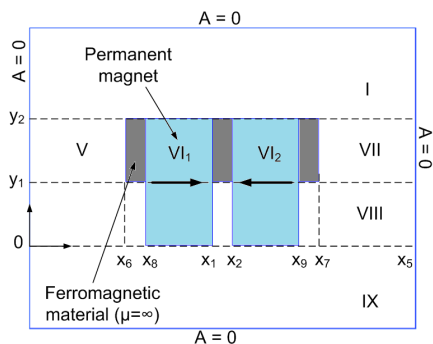


Figure 5. PMG model (Geometries B and C).

4. RESULTS AND VALIDATION

In order to show the accuracy of the analytical model, we compare the magnetic field distribution and levitation force obtained analytically with those obtained with the finite element method (FEM). The superconductor is modeled as a perfect diamagnetic material in the FEM with using a small relative permeability value (10^{-9}). For the ferromagnetic material which is considered linear (saturation is supposed negligible), a relative permeability of 10^7 has been used.

4.1. Flux Density and Levitation Force in HTSC-PMGs

4.1.1. Flux Density in HTSC-PMG: Geometry A

The main dimensions in millimeters of the studied HTSC-PMG maglev vehicle (Geometry A) are given in Fig. 6. With the known flux density distribution in all regions, the vertical force of the HTSC-PMG maglev vehicle can be determined. The force is calculated by means of Maxwell stress tensor at a closed path, along which the PMG is integrated. The integrals over the four lines of the closed path other than a line in the air gap (y_g) do not contribute significantly to the vertical force. So, the electromagnetic levitation force is expressed as follows:

$$F_y = \frac{L_u}{2\mu_0} \int_0^{x_5} \left(BIV_y(x, y_g)^2 - BIV_x(x, y_g)^2 \right) dx \quad (23)$$

where $L_u = 100$ mm is the z -direction length of the HTSC-PMG maglev vehicle.

The magnetic flux lines when the air-gap thickness is equal to 40 mm is shown in Fig. 7. One can see the distortion of the flux lines

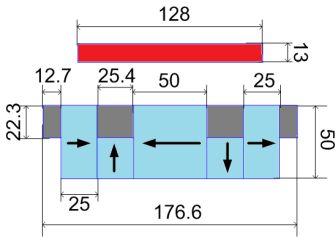


Figure 6. Dimensions in millimeters (mm) of the HTSC bulk and PMG: Geometry A.

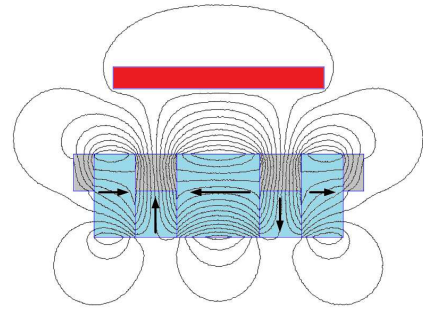


Figure 7. Magnetic flux lines in the HTSC-PMG.

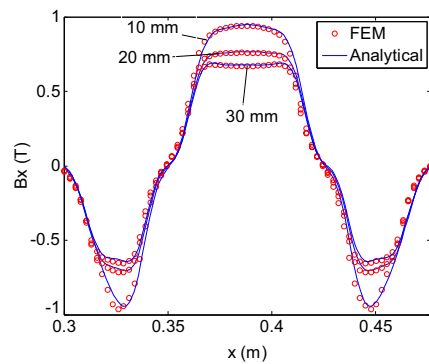
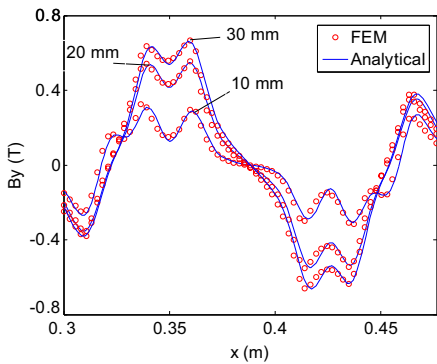


Figure 8. Analytical and finite element flux density components at $y_g = 55$ mm for three air-gap thickness.

at the location of the HTS bulk. The deviation of the field lines in the air-gap is the cause of the electromagnetic vertical force.

The magnetic flux density distribution in the y -direction B_y and x -direction B_x calculated at a height of 5 mm above the top surface of the PMG and for three air-gap thickness is shown in Fig. 8. At a working gap of 40 mm, the magnetic flux density components at three y_g (lines in the air gap) are shown in Fig. 9. It can be seen that the analytical results are extremely close to those issued from the FEM.

4.1.2. Flux Density in HTSC-PMG: Geometry B

Studied HTSC-PMG maglev vehicles (geometries B and C) have the dimensions shown in Fig. 10. The magnetic flux lines for both configurations (B and C) when the air-gap thickness is equal to 40 mm

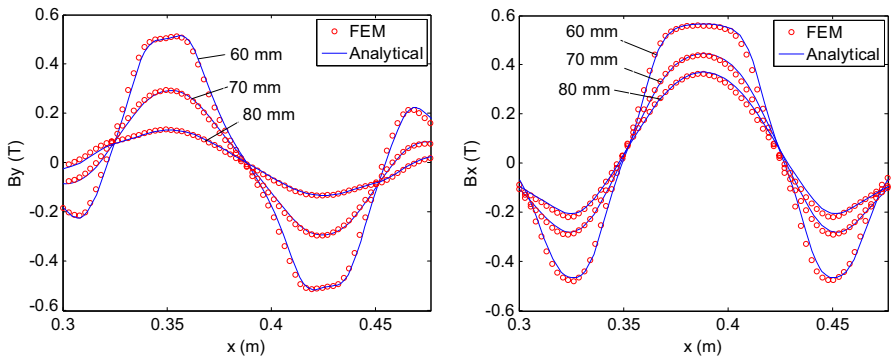


Figure 9. Analytical and finite element flux density components at three lines in the air-gap when working gap is equal to 40 mm.

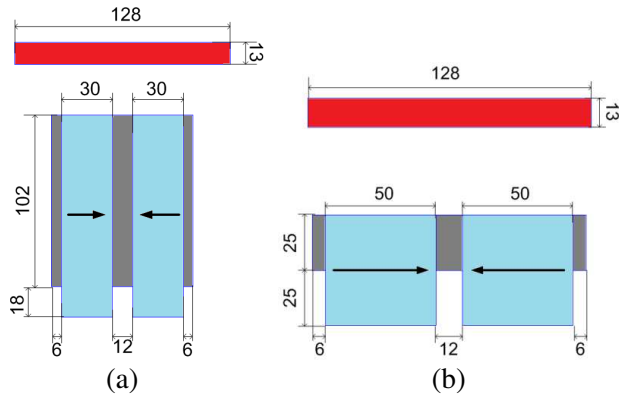


Figure 10. Dimensions in mm of the HTSC-PMG maglev vehicles. (a) Geometry B. (b) Geometry C.

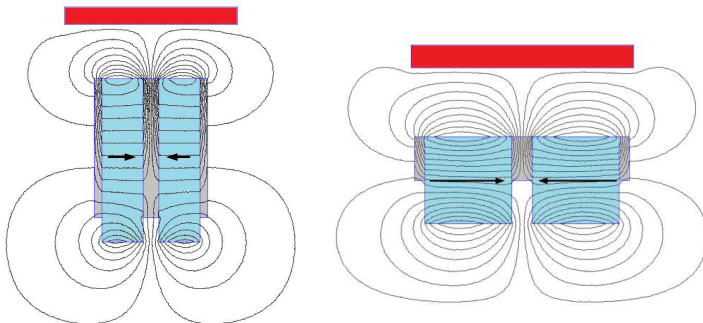


Figure 11. Magnetic flux lines in the two configurations of HTSC-PMG.

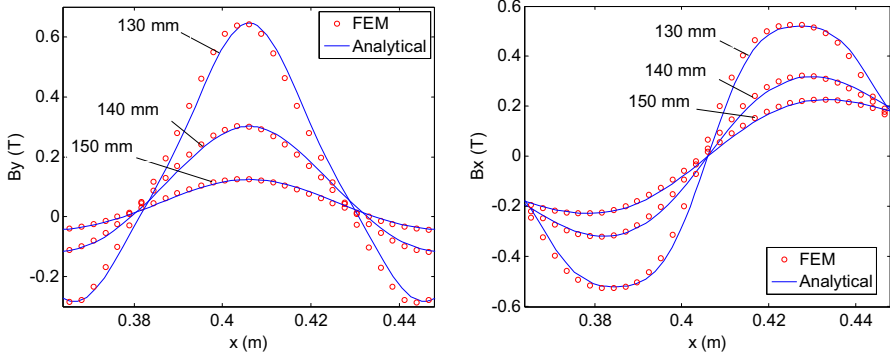


Figure 12. Analytical and finite element flux density components at three lines in the air-gap for a working gap of 40 mm.

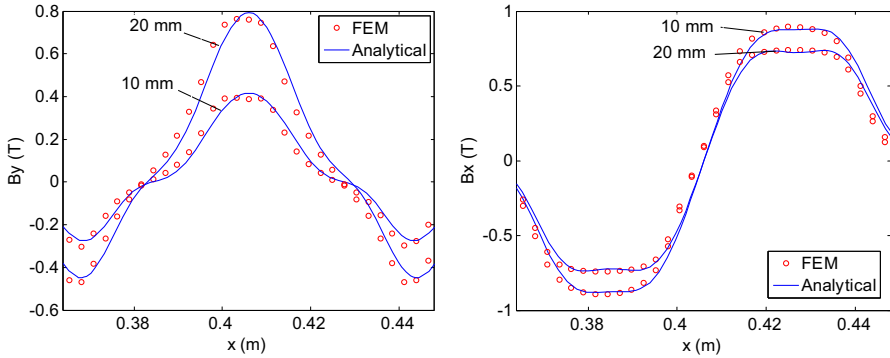


Figure 13. Analytical and finite element flux density components at $y_g = 125$ mm for two air-gap thickness in the y and x directions.

is shown in Fig. 11. One can see the deviation of equipotential lines in the air-gap at the vicinity of the superconducting bulk. The y -direction and x -direction components of the flux density distribution along the x -axis in region IV are shown in Figs. 12 and 13. The flux density distribution at three lines y_g in the air-gap when the gap is equal to 40 mm and for two air-gap thickness at a height of 5 mm above the top surface of the PMG are plotted in those figures. The analytical curves of B_x and B_y are in very good agreement with the FEM curves.

4.1.3. Flux Density in HTSC-PMG: Geometry C

This configuration is identical to Geometry B with a difference in the dimensions of permanent magnets and ferromagnetic material. The

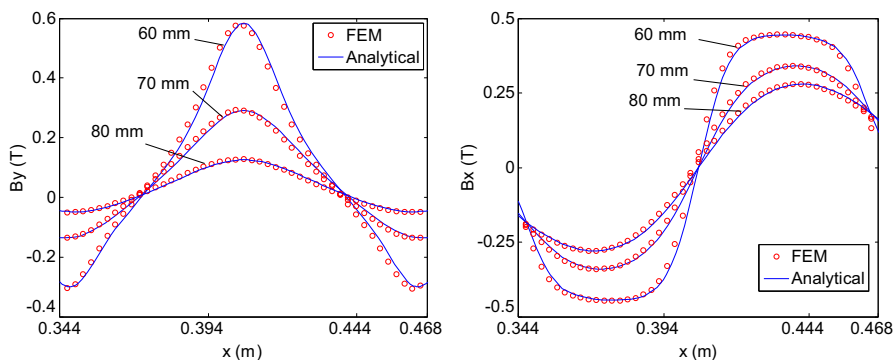


Figure 14. Analytical and finite element flux density components at three lines in the air-gap when the air-gap thickness is equal to 40 mm.

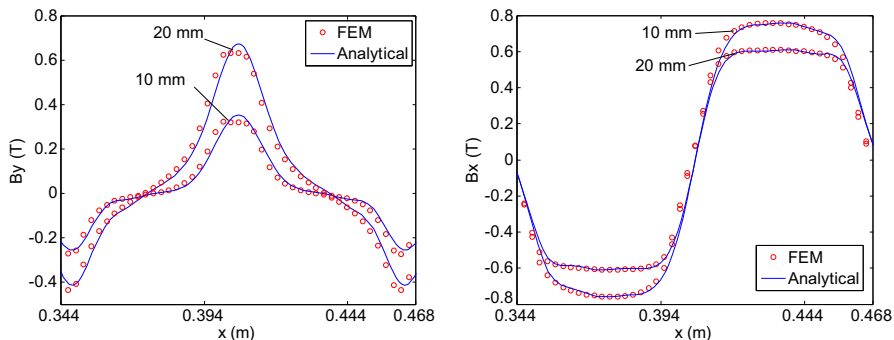


Figure 15. Analytical and finite element flux density components at $y_g = 55$ mm for two air-gap thickness in the y and x directions.

flux density distribution at three lines y_g in region IV when the air-gap thickness is equal to 40 mm and at a height of 5 mm above the top surface of the PMG for two air-gap thickness are shown in Figs. 14 and 15 respectively. The analytical curves of B_x and B_y agreed very well to the FEM curves.

The computational time requirements for magnetic field calculation in studied HTSC-PMGs topologies with analytical model and FEM are shown in Table 1. Analytical calculation time for used number of harmonics n , m , k and l (100, 100, 100 and 100) is greater when the number of subdomains increases. FEM computational time is approximately 13 times greater than analytical model. This is due to the meshing of spaces around the PMG and HTSC bulk which must be

Table 1. Computational time comparison between analytical model and FEM.

HTSC-PMG topologies	Analytical model (s)	FEM (s)	Mesh (nodes, elements)
Geometry A	12	128	646905, 1290394
Geometry B	10	153	719577, 1435546
Geometry C	10	131	706852, 1410081

important to improve the accuracy. The computational time increases also when the number of elements is higher for the same studied domain (surface).

4.1.4. Levitation Force

The developed vertical forces in function of air-gap thickness from the three configurations (A, B and C) of the HTSC-PMG maglev vehicles are shown in Fig. 16. Compared to the FEM simulations, one can see that the analytical calculation agrees very well when varying the air gap thickness. The best levitation performance is achieved by the Geometry A configuration.

4.2. Flux Density Created by the PMGs

4.2.1. Flux Density Created by the PMG Alone: Geometry A

Flux lines of Geometry A is shown in Fig. 17. The flux density components at three lines (y_g) above the PMG when the superconducting bulk is removed are shown in Fig. 18. Excellent agreement between analytical and FEM results is achieved.

4.2.2. Flux Density Created by the PMG Alone: Geometry B

Flux lines, in this case, are shown in Fig. 19. The flux density components at three y_g above the PMG are shown in Fig. 20. One can observe a very good agreement between analytical and finite elements predictions for both y -direction and x -direction components.

4.2.3. Flux Density Created by the PMG Alone: Geometry C

Flux lines created by the PMG are shown in Fig. 21. The magnetic field components at three y_g above the PMG are shown in Fig. 22. Excellent agreement between analytical and FEM results is also observed.

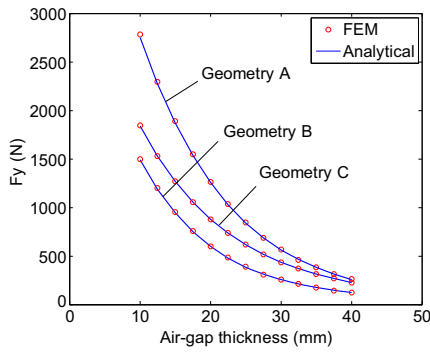


Figure 16. Analytical and finite element vertical forces at 5 mm above the PMG of the studied HTSC maglev vehicles in function of air-gap thicknesses.

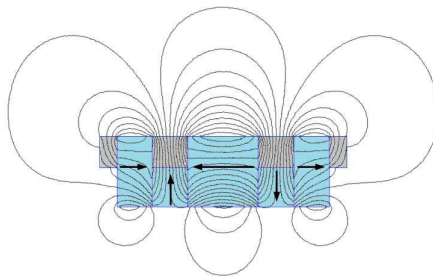


Figure 17. Flux lines created by the PMG without HTSC bulk (Geometry A).

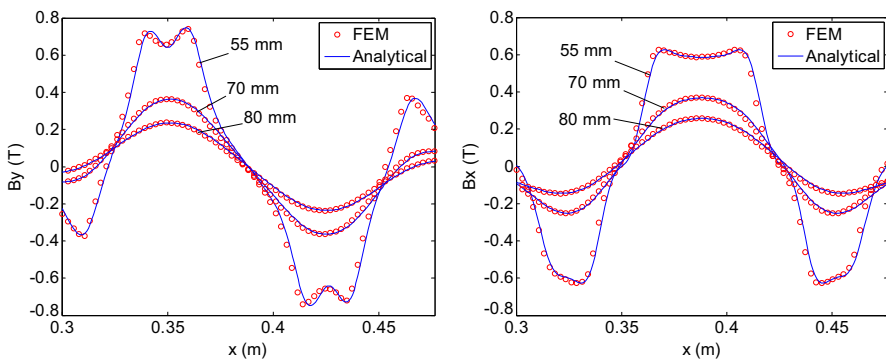


Figure 18. Analytical and finite element flux density components at three lines above the top surface of the PMG.

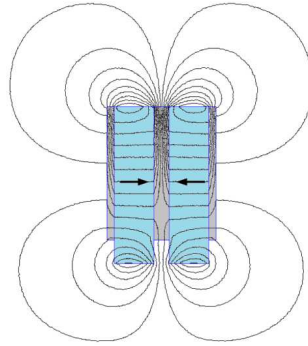


Figure 19. Flux lines created by the PMG without HTSC bulk (Geometry B).

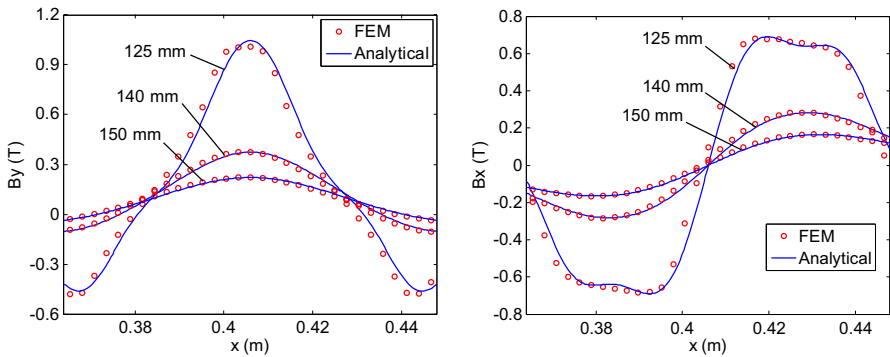


Figure 20. Analytical and finite element flux density components at three lines y_g above the top surface of the PMG.

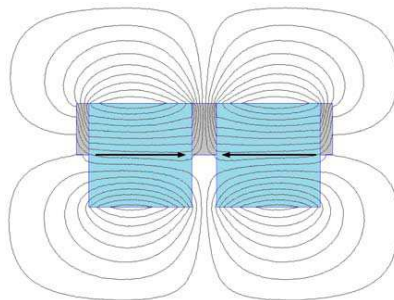


Figure 21. Flux lines created by the PMG without HTSC bulk (Geometry C).

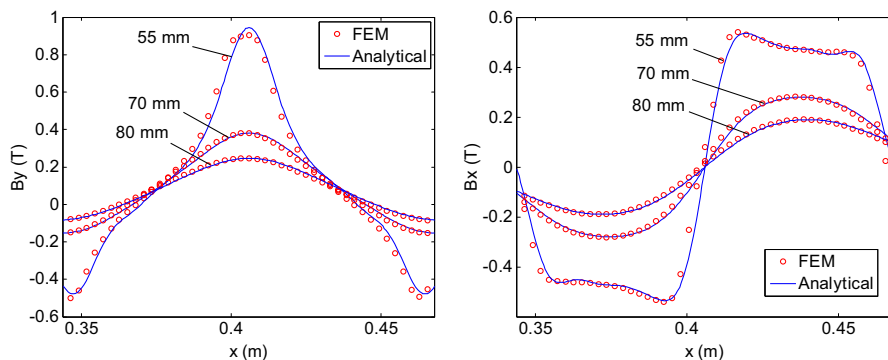


Figure 22. Analytical and finite element flux density components at three lines above the top surface of the PMG.

5. CONCLUSION

In this paper, a new analytical method to predict the air-gap magnetic field distribution and levitation force in three configurations of HTSC-PMG maglev vehicles has been presented. The Laplace and Poisson’s equations in Cartesian coordinates have been solved analytically by using the technique of the separation of variables. The solutions have been obtained using boundary and Fourier series expansion of continuity conditions between the different sub-domains. The different results presented in this paper have shown that the proposed analytical model is able to predict magnetic field distribution and levitation force of HTSC-PMG maglev vehicles with excellent precision. Hence, the analytical model developed in this paper can be used as a preliminary tool to investigate the influence of the design parameters such as HTS bulk width, air-gap thickness and PMG geometry dimensions.

The analytical model is extended to compute the magnetic field distribution generated by the three configurations of PMGs alone. The flux density generated by the PMGs alone and calculated analytically can be coupled to finite element method to determine levitation force for real HTSC-PMG systems.

APPENDIX A.

In terms of magnetic vector potential and magnetic excitation, the interface conditions between region I, region II and region III at $y = y_4$ (Fig. 1) which contain diamagnetic material lead to:

$$AI(x, y_4) = AII(x, y_4) + AIII(x, y_4) \tag{A1}$$

$$HI_x(x, y_4) = HII_x(x, y_4) \tag{A2}$$

$$HI_x(x, y_4) = HIII_x(x, y_4) \quad (\text{A3})$$

According to Fourier series expansion, from (A1), we obtain

$$\begin{aligned} C1_n e^{-\alpha y_4} &= \frac{2}{x_5} \sum_{k=1}^{\infty} \left(C2_k e^{\beta y_4} + C3_k e^{-\beta y_4} \right) G1 \\ &+ \frac{2}{x_5} \sum_{k=1}^{\infty} \left(C4_k e^{\lambda y_4} + C5_k e^{-\lambda y_4} \right) G2 \end{aligned} \quad (\text{A4})$$

where $G1 = \int_0^{x_3} \sin(\alpha x) \sin(\beta x) dx$ and $G2 = \int_{x_4}^{x_5} \sin(\alpha x) \sin(\lambda(x - x_4)) dx$.

Fourier series expansion of interface condition (A2) between regions I and II at $y = y_4$ gives

$$C2_k \beta e^{\beta y_4} - C3_k \beta e^{-\beta y_4} = -\frac{2}{x_3} \sum_{n=1}^{\infty} C1_n \alpha e^{-\alpha y_4} G1 \quad (\text{A5})$$

From interface condition (A3), we have

$$C4_k \lambda e^{\lambda y_4} - C5_k \lambda e^{-\lambda y_4} = -\frac{2}{x_5 - x_4} \sum_{n=1}^{\infty} C1_n \alpha e^{-\alpha y_4} G2 \quad (\text{A6})$$

The interface conditions between region IV, region II and region III at $y = y_3$ are:

$$AIV(x, y_3) = AII(x, y_3) + AIII(x, y_3) \quad (\text{A7})$$

$$HIV_x(x, y_3) = HII_x(x, y_3) \quad (\text{A8})$$

$$HIV_x(x, y_3) = HIII_x(x, y_3) \quad (\text{A9})$$

At $y = y_3$, Fourier series expansion of interface condition (A7) gives

$$\begin{aligned} C6_n e^{\alpha y_3} + C7_n e^{-\alpha y_3} &= \frac{2}{x_5} \sum_{k=1}^{\infty} \left(C2_k e^{\beta y_3} + C3_k e^{-\beta y_3} \right) G1 \\ &+ \frac{2}{x_5} \sum_{k=1}^{\infty} \left(C4_k e^{\lambda y_3} + C5_k e^{-\lambda y_3} \right) G2 \end{aligned} \quad (\text{A10})$$

Fourier series expansion of (A8) gives

$$C2_k \beta e^{\beta y_3} - C3_k \beta e^{-\beta y_3} = \frac{2}{x_3} \sum_{n=1}^{\infty} (C6_n \alpha e^{\alpha y_3} - C7_n \alpha e^{-\alpha y_3}) G1 \quad (\text{A11})$$

From (A9), we have

$$C4_k \lambda e^{\lambda y_3} - C5_k \lambda e^{-\lambda y_3} = \frac{2}{x_5 - x_4} \sum_{n=1}^{\infty} (C6_n \alpha e^{\alpha y_3} - C7_n \alpha e^{-\alpha y_3}) G2 \quad (\text{A12})$$

The continuity conditions between region IV; region V, region VI and region VII at $y = y_2$ which contain the ferromagnetic materials with infinitely permeability lead to:

$$AIV(x, y_2) = AV(x, y_2) \tag{A13}$$

$$AIV(x, y_2) = AVII(x, y_2) \tag{A14}$$

$$AIV(x, y_2) = AVI_j(x, y_2) \tag{A15}$$

$$HIV_x(x, y_2) = HV_x(x, y_2) + HVI_{xj}(x, y_2) + HVII_x(x, y_2) \tag{A16}$$

Fourier series expansion of interface condition (A13) between regions IV and V gives

$$C8_l e^{\psi y_2} + C9_l e^{-\psi y_2} = \frac{2}{x_6} \sum_{n=1}^{\infty} (C6_n e^{\alpha y_2} + C7_n e^{-\alpha y_2}) G3 \tag{A17}$$

From interface condition (A14) between regions IV and VII, we obtain

$$C12_l e^{\omega y_2} + C13_l e^{-\omega y_2} = \frac{2}{x_5 - x_7} \sum_{n=1}^{\infty} (C6_n e^{\alpha y_2} + C7_n e^{-\alpha y_2}) G4 \tag{A18}$$

where $G3 = \int_0^{x_6} \sin(\alpha x) \sin(\psi x) dx$ and $G4 = \int_{x_7}^{x_5} \sin(\alpha x) \cos(\omega(x - x_7)) dx$.

Fourier series expansion of interface condition (A15) between regions IV and VI leads to

$$C10_{j,0} + C11_{j,0} y_2 = \frac{1}{c_j} \sum_{n=1}^{\infty} (C6_n e^{\alpha y_2} + C7_n e^{-\alpha y_2}) \int_{g_j - \frac{c_j}{2}}^{g_j + \frac{c_j}{2}} \sin(\alpha x) dx \tag{A19}$$

$$C10_{j,m} e^{-\eta_j y_2} + C11_{j,m} e^{\eta_j y_2} = \frac{2}{c_j} \sum_{n=1}^{\infty} (C6_n e^{\alpha y_2} + C7_n e^{-\alpha y_2}) G5 \tag{A20}$$

where $G5 = \int_{g_j - \frac{c_j}{2}}^{g_j + \frac{c_j}{2}} \sin(\alpha x) \cos(\eta_j(x - g_j + \frac{c_j}{2})) dx$.

From (A16), we have

$$\begin{aligned} \frac{\alpha}{\mu_0} (C6_n e^{\alpha y_2} - C7_n e^{-\alpha y_2}) &= \frac{2}{x_5} \sum_{l=0}^{\infty} \frac{\psi}{\mu_0} (C8_l e^{\psi y_2} - C9_l e^{-\psi y_2}) G3 \\ + \frac{2}{x_5} \sum_{j=1}^3 \sum_{m=1}^{\infty} \frac{\eta_j}{\mu_0} &(-C10_{j,m} e^{-\eta_j y_2} + C11_{j,m} e^{\eta_j y_2}) G5 \end{aligned}$$

$$\begin{aligned}
& + \frac{2}{x_5} \sum_{j=1}^3 \frac{C11_{j,0}}{\mu_0} \int_{g_j - \frac{c_j}{2}}^{g_j + \frac{c_j}{2}} \sin(\alpha x) dx + \frac{2}{x_5} \sum_{l=0}^{\infty} \frac{\omega}{\mu_0} (C12_l e^{\omega y_2} - C13_l e^{-\omega y_2}) G4 \\
& - \frac{2}{x_5} \sum_{j=1}^3 M_{x,j} \int_{g_j - \frac{c_j}{2}}^{g_j + \frac{c_j}{2}} \sin(\alpha x) dx \tag{A21}
\end{aligned}$$

Interface conditions between region V, region VI, region VII and region VIII at $y = y_1$ lead to:

$$AVIII(x, y_1) = AV(x, y_1) \tag{A22}$$

$$AVIII(x, y_1) = AVII(x, y_1) \tag{A23}$$

$$AVIII(x, y_1) = AVI_j(x, y_1) \tag{A24}$$

$$HVIII_x(x, y_1) = HV_x(x, y_1) + HVI_{xj}(x, y_1) + HVII_x(x, y_1) \tag{A25}$$

Fourier series expansion of interface condition (A22) between regions VIII and V gives

$$C8_l e^{\psi y_1} + C9_l e^{-\psi y_1} = \frac{2}{x_6} \sum_{n=1}^{\infty} \left(C14_n e^{\alpha y_1} + C15_n e^{-\alpha y_1} - \mu_0 \frac{M y_n}{\alpha} \right) G3 \tag{A26}$$

From Fourier series expansion of interface condition (A23), we have

$$\begin{aligned}
& C12_l e^{\omega y_1} + C13_l e^{-\omega y_1} \\
& = \frac{2}{x_5 - x_7} \sum_{n=1}^{\infty} \left(C14_n e^{\alpha y_1} + C15_n e^{-\alpha y_1} - \mu_0 \frac{M y_n}{\alpha} \right) G4 \tag{A27}
\end{aligned}$$

Fourier series expansion of interface condition (A24) at $y = y_1$ leads to

$$\begin{aligned}
& C10_{j,0} + C11_{j,0} y_1 \\
& = \frac{1}{c_j} \sum_{n=1}^{\infty} \left(C14_n e^{\alpha y_1} + C15_n e^{-\alpha y_1} - \mu_0 \frac{M y_n}{\alpha} \right) \int_{g_j - \frac{c_j}{2}}^{g_j + \frac{c_j}{2}} \sin(\alpha x) dx \tag{A28} \\
& C10_{j,m} e^{-\eta_j y_1} + C11_{j,m} e^{\eta_j y_1} \\
& = \frac{2}{c_j} \sum_{n=1}^{\infty} \left(C14_n e^{\alpha y_1} + C15_n e^{-\alpha y_1} - \mu_0 \frac{M y_n}{\alpha} \right) G5 \tag{A29}
\end{aligned}$$

Interface condition (A25) gives

$$\begin{aligned} & \frac{C14_n \alpha e^{\alpha y_1} - C15_n \alpha e^{-\alpha y_1} - \mu_0 M x_n}{\mu_0} \\ &= \frac{2}{x_5} \sum_{l=0}^{\infty} \frac{\psi}{\mu_0} \left(C8_l e^{\psi y_1} - C9_l e^{-\psi y_1} \right) G3 - \frac{2}{x_5} \sum_{j=1}^3 M_{x,j} \int_{g_j - \frac{c_j}{2}}^{g_j + \frac{c_j}{2}} \sin(\alpha x) dx \\ &+ \frac{2}{x_5} \sum_{j=1}^3 \sum_{m=1}^{\infty} \frac{\eta_j}{\mu_0} \left(-C10_{j,m} e^{-\eta_j y_1} + C11_{j,m} e^{\eta_j y_1} \right) G5 \\ &+ \frac{2}{x_5} \sum_{l=0}^{\infty} \frac{\omega}{\mu_0} \left(C12_l e^{\omega y_1} - C13_l e^{-\omega y_1} \right) G4 \\ &+ \frac{2}{x_5} \sum_{j=1}^3 \frac{C11_{j,0}}{\mu_0} \int_{g_j - \frac{c_j}{2}}^{g_j + \frac{c_j}{2}} \sin(\alpha x) dx \end{aligned} \tag{A30}$$

where $M x_n = M1 x_n + M2 x_n + M3 x_n$.

The interface conditions between region VIII and region IX at $y = 0$ lead to:

$$AIX(x, 0) = AVIII(x, 0) \tag{A31}$$

$$HIX_x(x, 0) = HVIII_x(x, 0) \tag{A32}$$

At $y = 0$, the interface condition (A31) between regions IX and VIII gives

$$C16_n = C14_n + C15_n - \mu_0 \frac{M y_n}{\alpha} \tag{A33}$$

From interface condition (A32), we have

$$C16_n \alpha = \alpha (C14_n - C15_n) - \mu_0 M x_n \tag{A34}$$

The system of 18 Equations (A4), (A5), (A6), (A10), (A11), (A12), (A17), (A18), (A19), (A20), (A21), (A26), (A27), (A28), (A29), (A30), (A33) and (A34) permit to calculate the 18 coefficients $C1_n$, $C2_k$, $C3_k$, $C4_k$, $C5_k$, $C6_n$, $C7_n$, $C8_l$, $C9_l$, $C10_{j,0}$, $C10_{j,m}$, $C11_{j,0}$, $C11_{j,m}$, $C12_l$, $C13_l$, $C14_n$, $C15_n$ and $C16_n$ with a given number of harmonics for n , k , m and l .

REFERENCES

1. Zhang, J., Y. Zeng, J. Cheng, and X. Tang, "Optimization of permanent magnet guideway for HTS maglev vehicle with

- numerical methods,” *IEEE Trans. on Applied Superconductivity*, Vol. 18, No. 3, 1681–1686, September 2008.
2. Deng, Z., J. Zheng, J. Li, G. Ma, Y. Lu, Y. Zhang, S. Wang, and J. Wang, “Superconducting bulk magnet for maglev vehicle: Stable levitation performance above permanent magnet guideway,” *Materials Science and Engineering B*, Vol. 151, 117–121, Elsevier, 2008.
 3. Liu, L., J. Wang, S. Wang, L. Wang, and J. Li, “Flux concentrator optimization of PMG for high-temperature superconducting maglev vehicle system,” *J. Low Temperature Physics*, Vol. 157, 67–72, Springer, 2009.
 4. Del-Valle, N., A. Sanchez, C. Navau, and D. X. Chen, “Magnet guideways for superconducting maglevs: Comparison between Halbach-type and conventional arrangements of permanent magnets,” *J. Low Temperature Physics*, Vol. 162, 62–71, Springer, 2011.
 5. Dias, D. H. N., G. G. Sotelo, F. Sass, E. S. Motta, R. de Andrade, Jr., and R. M. Stephan, “Dynamical tests in a linear superconducting magnetic bearing,” *Physics Procedia*, Vol. 36, 1049–1054, 2012.
 6. Stephan, R. M., R. Nicolsky, M. A. Neves, A. C. Ferreira, R. de Andrade, Jr., M. A. Cruz Moreira, M. A. Rosario, and O. J. Machado, “A superconducting levitation vehicle prototype,” *Physica C*, Vol. 408–410, 932–934, 2004.
 7. Jin, J., L. Zheng, Y. Guo, W. Xu, and J. Zhu, “Analysis and experimental validation of an HTS linear synchronous propulsion prototype with HTS magnetic suspension,” *Physica C*, Vol. 471, 520–527, 2011.
 8. Werfel, F. N., U. Floegel-Delor, R. Rothfeld, T. Riedel, D. Wippich, B. Goebel, and P. Schirrmeister, “Bulk superconductors in mobile application,” *Physics Procedia*, Vol. 36, 948–952, 2012.
 9. Werfel, F. N., U. Floegel-Delor, R. Rothfeld, T. Riedel, B. Goebel, D. Wippich, and P. Schirrmeister, “Superconductor bearings, flywheels and transportation,” *Superconductor Science and Technology*, Vol. 25, 1–16, 2012.
 10. Malé, G., T. Lubin, S. Mezani, and J. Lévêque, “Analytical calculation of the flux density distribution in a superconducting reluctance machine with HTS bulks rotor,” *Mathematics and Computers in Simulation*, 1–14, Elsevier, 2013.
 11. Motta, E. S., R. M. Stephan, J. H. Norman, H. C. Ramos, G. G. Sotelo, and D. H. N. Dias, “Optimization of superconducting magnetic rail using a feasible direction interior point algorithm,”

- International Conference on Engineering Optimization*, 1–5, Rio de Janeiro, June 2008.
12. Li, W., K. T. Chau, and J. Li, "Simulation of a tubular linear magnetic gear using HTS bulks for field modulation," *IEEE Trans. on Applied Superconductivity*, Vol. 21, No. 3, 1167–1170, June 2011.
 13. Motta, E. S., D. H. N. Dias, G. G. Sotelo, H. O. C. Ramos, J. H. Norman, and R. M. Stephan, "Optimization of a linear superconducting levitation system," *IEEE Trans. on Applied Superconductivity*, Vol. 21, No. 5, 3548–3554, October 2011.
 14. Barba, P. D. and R. Palka, "Optimization of the HTSC-PM interaction in magnetic bearings by a multiobjective design," *Studies in Computational Intelligence*, Vol. 119, 83–90, SCI, Springer, 2008.
 15. Palka, R., "Modeling of high temperature superconductors and their practical applications," *International Compumag Society Newsletter*, Vol. 12, No. 3, 3–12, November 2005.
 16. Lu, Y., X. Bai, Y. Ge, and J. Wang, "Influence of thickness on the levitation force of high-T_c bulk over a permanent magnetic guideway with numerical method," *J. Supercond Nov. Magn.*, Vol. 24, 1967–1970, 2011.
 17. Dias, D. H. N., E. S. Motta, G. G. Sotelo, and R. Andrade, Jr., "Experimental validation of field cooling simulations for linear superconducting magnetic bearings," *Superconductor Science and Technology*, Vol. 23, 1–6, 2010.
 18. Dias, D. H. N., E. S. Motta, G. G. Sotelo, R. Andrade, R. M. Stephane, L. Kuehn, O. Haas, and L. Schultz, "Simulations and tests of superconducting linear bearings for a MAGLEV prototype," *IEEE Trans. on Applied Superconductivity*, Vol. 19, No. 3, 2120–2123, June 2009.
 19. Jin, J. X., L. H. Zheng, Y. G. Guo, J. G. Zhu, C. Grantham, C. C. Sorrel, and W. Xu, "High-temperature superconducting linear synchronous motors integrated with HTS magnetic levitation components," *IEEE Trans. on Applied Superconductivity*, Vol. 22, No. 5, 5202617, October 2012.
 20. Ma, G.-T., "Considerations on the finite-element simulation of high-temperature superconductors for magnetic levitation purposes," *IEEE Trans. on Applied Superconductivity*, Vol. 23, No. 5, 3601609, October 2013.
 21. Wang, S., J. Zheng, H. Song, X. Wang, and J. Wang, "Experiment and numerical calculation of high temperature superconducting maglev," *IEEE Trans. on Applied Superconductivity*, Vol. 15,

- No. 2, 2277–2280, June 2005.
22. Zheng, J., H. Song, J. Wang, S. Wang, M. Liu, and H. Jing, “Numerical method to the excited high- t_c superconducting levitation system above the NdFeB guideway,” *IEEE Trans. on Magnetics*, Vol. 42, No. 4, 947–950, April 2006.
 23. Dias, D. H. N., G. G. Sotelo, and R. Andrade, “Study of the lateral force behavior in a field cooled superconducting linear bearing,” *IEEE Trans. on Applied Superconductivity*, Vol. 21, No. 3, 1533–1537, June 2011.
 24. Costamagna, E., P. D. Barba, M. E. Mognaschi, and A. Savini, “Fast algorithms for the design of complex-shape devices in electromechanics,” *Computational Methods for Electrical Devices Design*, Vol. 327, 59–86, SCI, Springer, 2010.
 25. Boughrara, K., T. Lubin, R. Ibtouen, and N. Benallal, “Analytical calculation of parallel double excitation and spoke-type permanent-magnet motors; simplified versus exact model,” *Progress In Electromagnetics Research B*, Vol. 47, 145–178, 2013.
 26. Lubin, T., K. Berger, and A. Rezzoug, “Inductance and force calculation for axisymmetric coil systems including an iron core of finite length,” *Progress In Electromagnetics Research B*, Vol. 41, 377–396, 2012.
 27. Sotelo, G. G., D. H. N. Dias, R. Andrade, Jr., R. M. Stephane, N. Del-Valle, A. Sanchez, C. Navau, and D. Chen, “Experimental and theoretical levitation forces in a superconducting bearing for a real-scale maglev system,” *IEEE Trans. on Applied Superconductivity*, Vol. 21, No. 5, 3532–3540, October 2011.
 28. Sotelo, G. G., D. H. N. Dias, O. J. Machado, E. D. David, R. Andrade, Jr., R. M. Stephane, and G. C. Costa, “Experiments in a real scale maglev vehicle prototype,” *Journal of Physics: Conference Series*, Vol. 234, 032054, 1–7, 2010.
 29. Sotelo, G. G., R. de Andrade, Jr., D. H. N. Dias, A. C. Ferreira, F. Costa, O. J. Machado, R. A. H. de Oliveira, M. D. A. Santos, and R. M. Stephan, “Tests with one module of the Brazilian Maglev-Cobra vehicle,” *IEEE Trans. on Applied Superconductivity*, Vol. 23, No. 3, 3601204, June 2013.
 30. Wang, J., S. Wang, and J. Zheng, “Recent development of high temperature superconducting maglev system in China,” *IEEE Trans. on Applied Superconductivity*, Vol. 19, No. 3, 2142–2147, June 2009.
 31. Meeker, D. C., *Finite Element Method Magnetics*, Ver. 4.2 (April 1, 2009 Build), [Online], Available: <http://www.femm.info>.